



RESEARCH LETTER

10.1002/2017GL075032

Key Points:

- We identify a high-velocity slab-like fragment beneath the southeastern U.S.
- The fragment has a 100 km thick core with relatively sharp edges on both sides
- The anomaly may be associated with the eclogitized Hess conjugate

Supporting Information:

- Supporting Information S1

Correspondence to:

J. Y.-T. Ko,
justinko@caltech.edu

Citation:

Ko, J. Y.-T., Helmberger, D. V., Wang, H., & Zhan, Z. (2017). Lower mantle substructure embedded in the Farallon Plate: The Hess conjugate. *Geophysical Research Letters*, 44, 10,216–10,225. <https://doi.org/10.1002/2017GL075032>

Received 20 JUL 2017

Accepted 17 SEP 2017

Accepted article online 29 SEP 2017

Published online 21 OCT 2017

Lower Mantle Substructure Embedded in the Farallon Plate: The Hess Conjugate

Justin Yen-Ting Ko¹ , Don V. Helmberger¹, Huilin Wang¹ , and Zhongwen Zhan¹ 

¹Seismological Laboratory, California Institute of Technology, Pasadena, CA, USA

Abstract The morphologies of subducted remnants in the lower mantle are essential to our understanding of the history of plate tectonism. Here we image a high-velocity slab-like (HVSL) anomaly beneath the southeastern U.S. using waveforms from five deep earthquakes beneath South America recorded by the USArray. In addition to travel time anomalies, the multipathing of *S* and *ScS* phases at different distances are used to constrain the HVSL model. We jointly invert *S* and *ScS* traveltimes, amplitudes, and waveform complexities to produce a best fitting block model characterized by a rectangular shape with a 2.5% *S* wave velocity increase and tapered edges. While the Farallon slab is expected to dip primarily eastward, the HVSL structure apparently dips 40° to 50° to the SE and appears to be related to the eclogitized Hess conjugate.

1. Introduction

The improved imaging of structures in the lower mantle could provide critical constraints on mantle dynamics and help to understand the evolutionary processes that govern surface tectonics (e.g., Biryol et al., 2016; Jones et al., 1994; Liu et al., 2008; Porritt et al., 2014; Saleeby et al., 2012; Schmandt & Lin, 2014). Numerous studies have produced consistent images of high-velocity anomalies in the deep mantle (depths >1,000 km) beneath the eastern U.S. that might represent remnants of the Farallon Plate that was subducted along the western margin of North America starting in the Cretaceous (Figure 1) (e.g., Bunge & Grand, 2000; Grand, 2002; Ritsema et al., 2011; Simmons et al., 2012). However, the origins of high-velocity fragments within the mantle transition zone (~300–1,000 km) are still under debate. Sigloch and Mihalynuk (2013) proposed a scenario assuming a normal rate of slab sinking, that is, 2 cm/yr (Grand, 2002), and interpreted the fast anomalies as originating from intraoceanic subduction to the west. Liu et al. (2010) discussed the roles of oceanic plateau subduction in the generation of these fragments and the associated Laramide orogeny by combining plate kinematic reconstructions with the inverse modeling of mantle convection. In contrast, Biryol et al. (2016) argued that fast anomalies may reflect dense lithospheric mantle that has been partially removed due to delamination.

The controversy presented herein is at least partly due to the inconsistent tomographic images provided by different studies. Lu and Grand (2016) concluded that tomographic models generated without correcting for slab effects in the source region could map errors reaching 0.5% into the predicted shear wave velocity anomalies. Moreover, models produced via tomographic methods may underestimate the strengths of such anomalies. For example, the velocity perturbations representative of slab-like structures are generally smaller in tomographic images than in those inferred from recent waveform modeling endeavors (Zhan et al., 2014).

The modeling of broadband waveforms can provide complimentary constraints on the velocity perturbations, sharpness, and geometries of various anomalies (e.g., Chu, Helmberger, et al., 2012; Silver & Chan, 1986; Song & Helmberger, 2007a, 2007b; Sun & Helmberger, 2011). In particular, for a slab-like structure, we would expect *S* and *ScS* waves to sample the structure differently, as displayed in Figures S2 and S3, where we present some sensitivity tests for a variety of geometries. The synthetics were generated with a new finite difference method (Li, Helmberger, et al., 2014) and are discussed in the supporting materials (Helmberger et al., 1985; Vidale et al., 1985; Levander, 1988; Chen et al., 2006; Tromp et al., 2008; Tromp et al., 2010; Li, Sun, et al., 2014). When raypaths are aligned with the edge of a slab, the associated multipathing produces waveform distortions, travel time jumps, and amplitude variations. These waveform complexities depend on both the source depth and source duration and can lead to a complicated analysis.

We explore the extensive and dense raypath coverage provided by the USArray over the past decade using deep earthquakes generated beneath South America to investigate shear-wave velocity anomalies beneath

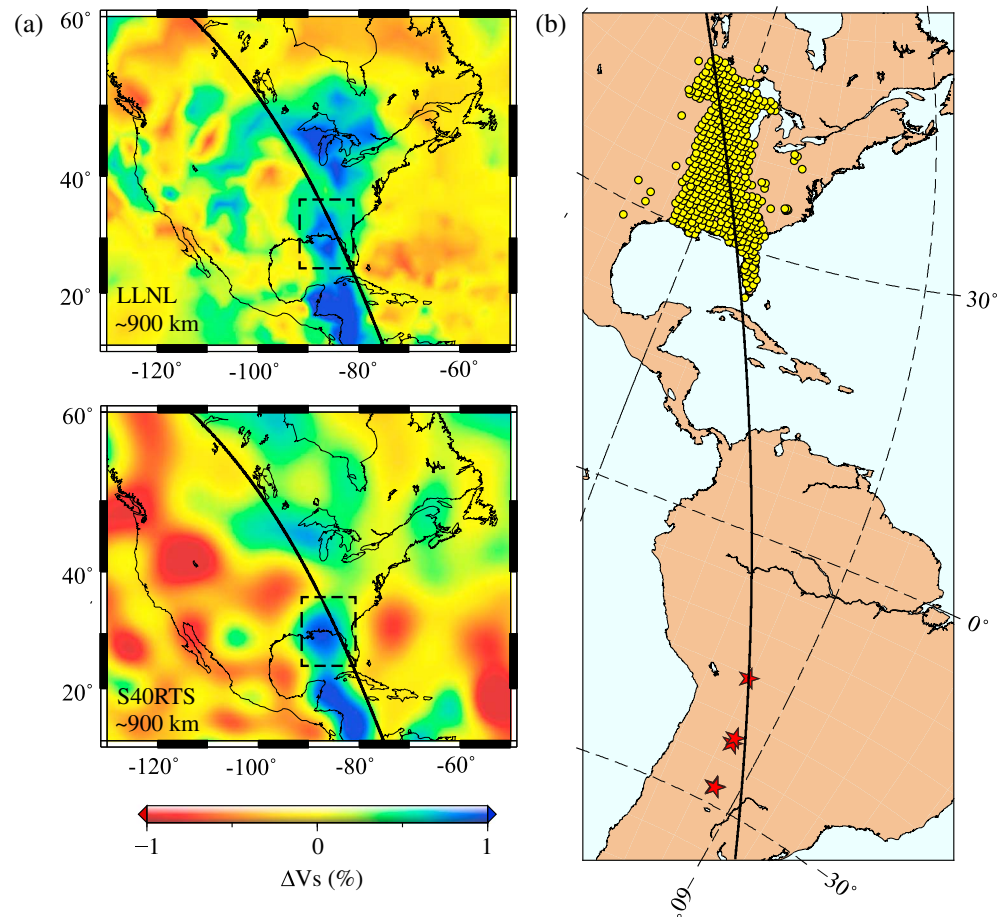


Figure 1. Map views of tomographic models and the event station configuration. (a) Map view of the LLNL (Simmons et al., 2015) and S40RTS (Ritsema et al., 2011) models at a depth of ~ 900 km displaying tomographic images of the fast fragment (dashed box) beneath the southeastern U.S. The black line indicates the great circle path used to invert the optimal 2-D model in this study. (b) Distribution of events (red stars) and stations (yellow circles) used in this study.

the southeastern U.S. (Figure 1b). Accordingly, we jointly model S and ScS traveltimes, amplitudes, and waveform shapes to establish the velocity model and morphology of the high-velocity slab-like (HVSL) anomaly beneath the southeastern U.S. and the northern Gulf of Mexico.

2. Data and Measurements

The deployment of the USArray between 2011 and 2013 provides unprecedented raypath coverage beneath the southeastern U.S. (Figure 1). Consequently, we examined recordings from events with magnitudes of 5.5 or greater from the South American subduction zone that occurred during this period of deployment. Only events with focal depths exceeding 300 km are selected to avoid interference between depth phases and triplicate arrivals as well as slab contributions on the source side. Nearly 4,000 broadband displacement waveforms from five events (Table S1) recorded by both USArray and permanent stations in North America were collected for further data processing and to apply quality control measures to mitigate noise issues. All of the horizontal component waveforms are deconvolved with the instrument response, rotated into a radial-transverse coordinate system, and high-pass filtered with a cutoff frequency of 0.01 Hz. Since the earthquake mechanisms exhibited favorable SH wave radiation patterns toward the north, only SH wavefields are addressed herein. The final dataset consists of 3,328 shear wave records after applying quality control measures based on the signal-to-noise ratio (S/N) threshold > 10 , which is defined as the maximum amplitude of the S wave divided by the standard deviation of the background noise within a 40 s window prior to the S wave arrival.

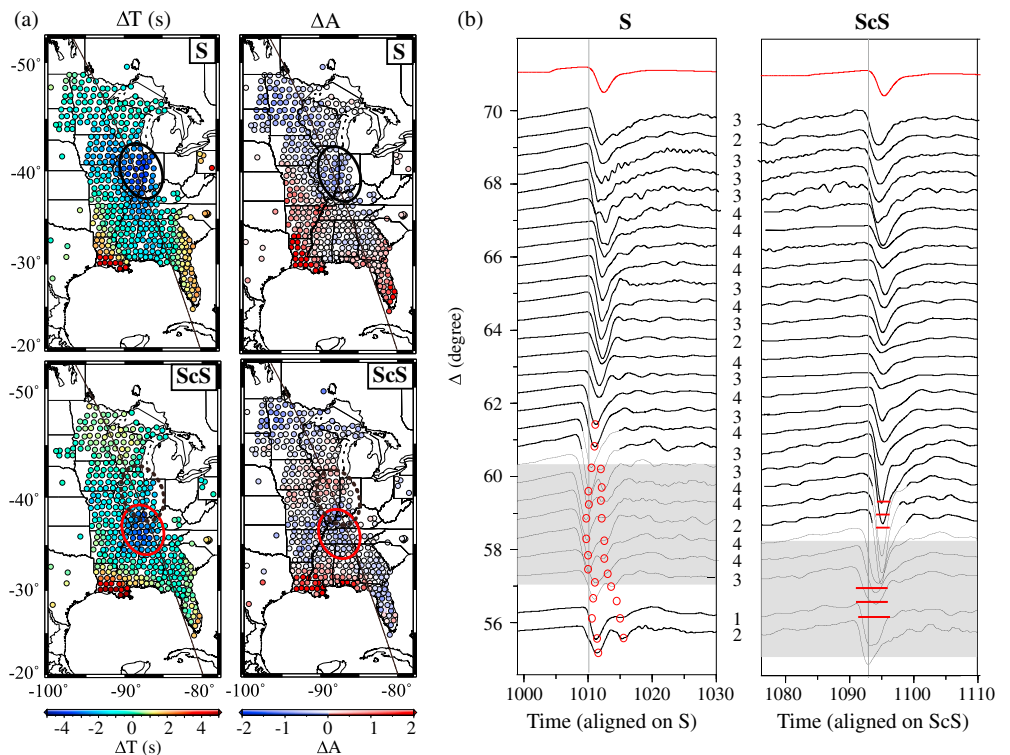


Figure 2. Displays of the data measurements and stacked waveforms. (a) An example event (2012.149) showing the traveltime and amplitude anomalies relative to the PREM. All measurements are plotted at the station locations. For the traveltime delay maps, colder and warmer colors indicate advanced and delayed arrivals of the S and ScS phases, respectively. For the amplitude anomalies, the blue and red colors represent the reduced and amplified amplitudes of the S and ScS phases, respectively. The area with a fast anomaly and a reduced amplitude is demarcated with black (S) and red (ScS) circles. To better compare the locations of the S and ScS anomalies, we plot the S wave anomaly as a dashed black circle on the ScS anomaly map. (b) Record sections from the 2011.326 event spanning an azimuthal range of 3° along the great circle path (black line) shown in Figure 2a. The first and second columns display the S and ScS waveforms, respectively, stacked in distance bins of 0.5°. The number of stations included in each bin is labeled at the bin center. The red traces plotted at the tops of the columns are the source wavelets obtained from the stacked data at distances of less than 70°. The shaded regions indicate the presence of strong waveform distortions that are caused by mantle heterogeneities. The red dots and red bars indicate multipath arrivals and broadened waveforms, respectively.

We measure the relative amplitudes (ΔA) and differential traveltimes (ΔT) by cross correlating the S and ScS waves between the data and synthetics computed using the direct solution method (DSM) (Kawai et al., 2006), the PREM (Preliminary Reference Earth Model) (Dziewonski & Anderson, 1981), and source solutions from the GCMT (Global Centroid Moment Tensor) catalog (Dziewonski et al., 1981; Ekström et al., 2012). The pattern of travel time and the amplitude anomalies for the S and ScS waves recorded from the five events were mostly consistent. As shown in Figure 2a, the fast anomaly for event 2012.149 (Table S1 in the supporting information) is represented within the maps as a region with a negative ΔT and a shift of the ScS phase of $\sim 2^\circ$ to the south relative to the S wave. This shift demonstrates the different sensitivities of the direct S and ScS phases to the structure as a function of their different ray parameters, which can be utilized as a useful tool for probing the geometry of the anomaly. Moreover, the distribution of the fast anomaly along with its reduced amplitude (Figure 2a) implies the presence of strong wavefield distortions due to multipathing effects.

To demonstrate how multipathing phenomena can be produced, we select an event with a short source duration and stack the seismic records in 0.5° distance bins. Traveltime differences of ~ 4 s relative to predictions from the PREM and the significant broadening and complexity of the stacked S waveforms between distances of 57° and 60° are observed (Figure 2b). Similar features are also observed in the ScS stacked waveforms, albeit with an $\sim 2^\circ$ shift to the south. Note that this shift between the S and ScS phases is observed among all of the synthetics (Figures S2 and S3) and is indicative of a SE dipping structure. The distortion

patterns between the *S* and *ScS* phases is highly dependent upon the slab shape. Moreover, significant shifts in the *S* waveform complexities among various events are expected because of changes in the epicentral distance and source duration.

The azimuthal variations in the traveltime delays suggest that the HVSL structure is approximately 550 km wide (perpendicular to the raypath) (Figure 2a). Off-great-circle diffractions might also produce multipathing effects if the seismic wavefield propagates across sharp velocity boundaries (i.e., the western and eastern edges of the anomalous region). Since the radius of the first Fresnel zone is ~ 150 km for a shear wave with a 5 s period at a depth of 500 km, record sections formed from events traversing the middle of the anomalous region should be relatively free of off-great-circle propagation effects. We acknowledge that 3-D effects should be considered to better understand the detailed morphology of such a high-velocity anomaly, but the lack of deep events from the east (i.e., the Atlantic) limits the availability of record sections for this type of waveform study. However, we will demonstrate that much of the waveform complexity from this data set can be explained by an idealized 2-D block (i.e., an HVSL), as discussed in the following sections.

3. Waveform Modeling and Inversion

We attempt to model a 2-D corridor (introduced in Figure 1) to fit the observed travel times, amplitudes, and waveform shapes. We use the LLNL (Lawrence Livermore National Laboratory) model (Simmons et al., 2015) as the background model, which explains the traveltime behaviors well but cannot account for the observed amplitudes and waveforms (Figure S4). Moreover, while the tomographic models show an HVSL structure that is sampled by *S* waves near 60° (Figure S1), those same models are too smooth to effectively display the observed effects of multipathing (Figure 2b). To investigate the possible morphology of the anomaly, we establish an inversion (illustrated in Figure 3a and Table S2) that grid searches for the best fitting rectangular block using six model parameters: the dip angle, velocity perturbation, sharpness, width, length, and top boundary (TB) depth. This rectangular block is inserted into the LLNL model, and the velocity fluctuations are added to the existing velocity anomalies inside the block. We also allow the TB depth to vary and give the edges of the block a transition zone characterized by a sharpness value. In summary, we have portrayed a smoothed rectangular block with just six parameters. All of the synthetics involved in the grid search procedure are calculated using an efficient graphics processing unit-based 2-D finite difference (FD) method (Li, Helmberger, et al., 2014) with source solutions from the GCMT catalog. We set the FD grid size to 1 km and the time step to 0.01 s to ensure that the simulated wavefield is accurate up to 1 Hz.

3.1. Sensitivities and Trade-Offs Between the Model Parameters

We carried out a series of sensitivity experiments using simulated waveforms and data measures to clarify their effective constraints on each model parameter. As shown in Figure S5, due to the deviations in ray parameters between the *S* and *ScS* waves, the changes in dip angle of the anomaly significantly altered the traveltime and amplitude patterns as well as the shapes of the *S* and *ScS* waveforms (as shown in Figure S2). An increase in the anomaly width will broaden the anomalous patterns (Figure S3), and variations in its length will perturb the predicted traveltime and amplitude curves at nearer and farther distances, respectively, for the *S* and *ScS* phases. Changes in the TB depth of the anomaly will produce similar effects in terms of shifts in the observed distances of the anomalous region relative to various dip angles (Figures S2 and S3). In short, trade-offs between the model parameters are inevitable while exploring the six-parameter model space all at once. To mitigate these trade-offs, we jointly model the travel times, amplitudes, and waveform complexities of the *S* and *ScS* phases derived from five events at different distances. Combining a variety of event-station ray configurations with different sensitivities in the inversion can largely improve the resulting resolution and eliminate potential trade-offs.

3.2. Inversion Methodology and Results

Benefiting from the highly efficient FD program, we compute large numbers of Green's functions to form a library of idealized slab models (see Table S2). We grid search for the six parameters by minimizing the differences in the travel times, amplitudes, and waveforms between the synthetics and the data. The cost function ε is defined as the sum of the L2 norm of the misfit errors for different events as follows (Ko et al., 2017):

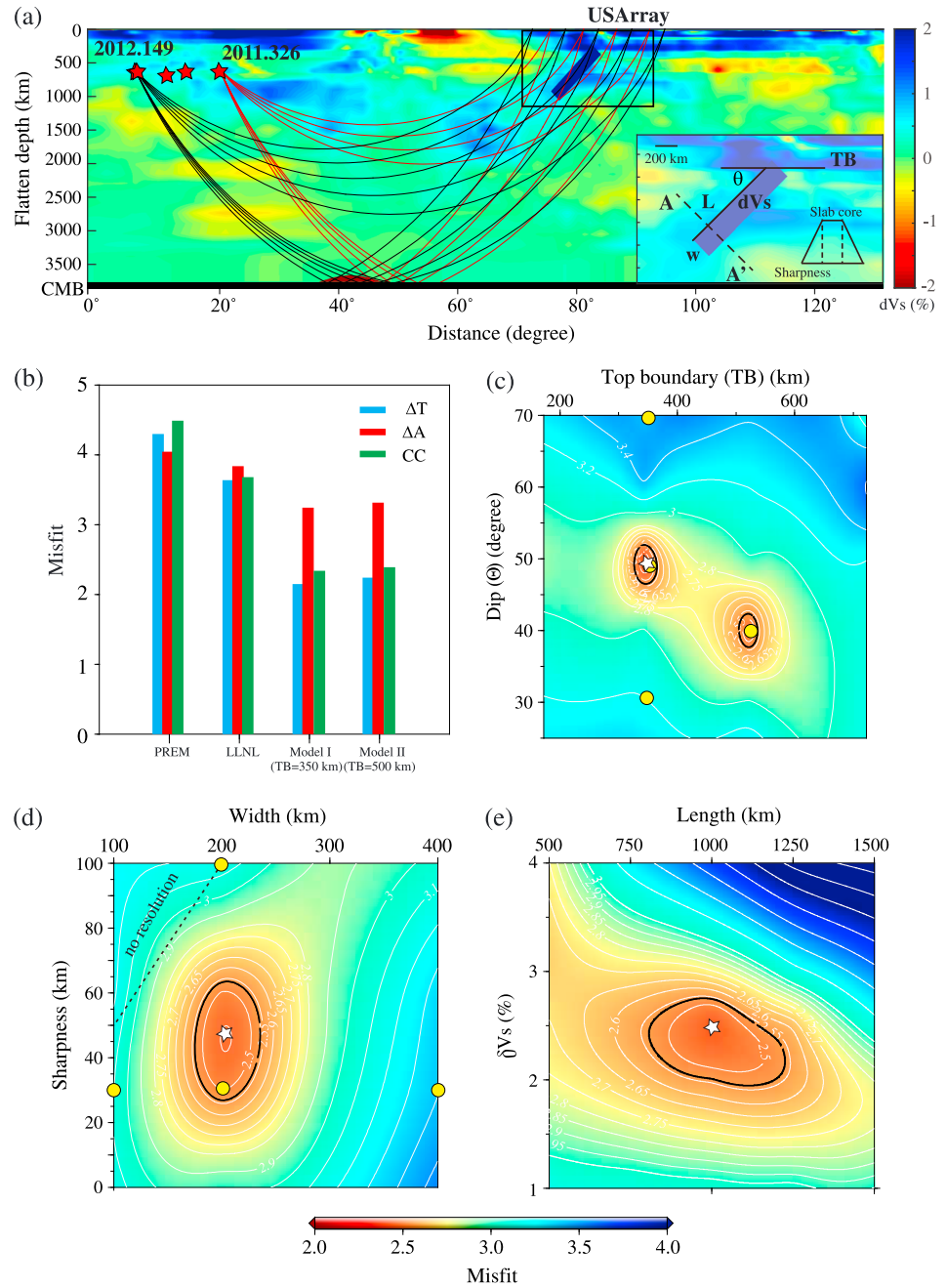


Figure 3. The 2-D model and inversion results. (a) The model layout for the 2-D waveform simulation showing the five event locations (red stars) and raypaths from the nearest (red) and the most distant (black) events. The inset shows the model parameters used to describe the geometry of the fragment, including the dip angle, width, length, top boundary (TB), sharpness, and velocity perturbation of the fragment. Note that the top and the bottom of this 2-D block have tapered sides. Cross-section AA' represents the profile used to estimate the velocity gradient shown in Figure 5. (b) Histogram of the misfit functions estimated using the 1-D PREM, the 3-D LLNL model, and our idealized HVSL models. The misfit maps with contours demonstrate the values of the cost function with different trial model variables: (c) the dip angle and TB, (d) the sharpness and width, and (e) the velocity perturbation and length. The white stars indicate the optimal solutions, while the yellow dots are the results from the models whose waveform sections are shown in Figures S2 and S3. The black contours delineate the regions in which the misfit deviates from the global minimum by less than 5%.

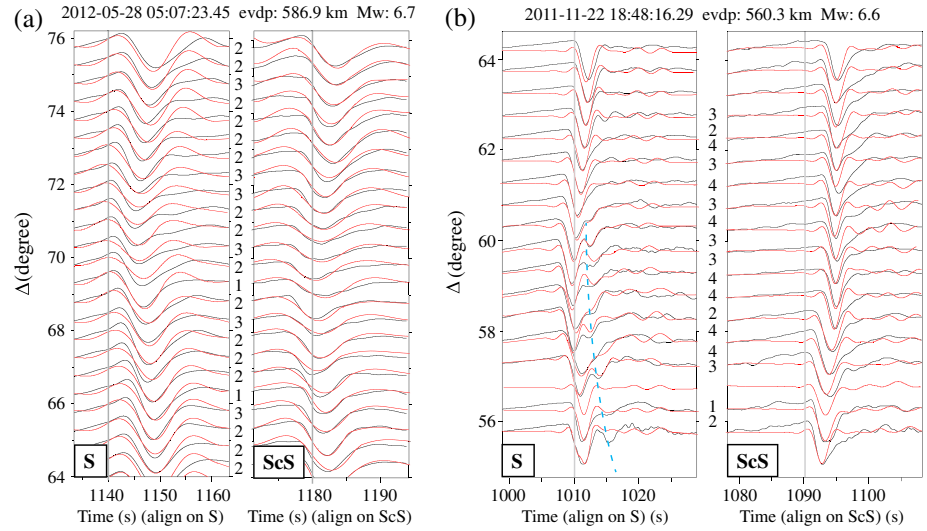


Figure 4. The fitting results for events (a) 2012.149 and (b) 2011.326. The black lines are the observed waveforms, and the red lines indicate the synthetic waveforms obtained using our preferred model. Due to differences in the source durations of the earthquakes, the synthetic waveforms are low-pass filtered with cutoff frequencies of 0.1 Hz (Figure 4a) and 0.4 Hz (Figure 4b). The dashed blue line shown in Figure 4b delineates the multipath arrivals.

$$\varepsilon = \sum_{j=1}^5 \varphi_j \varphi = \sum_{i=S, ScS} \left\| \frac{\Delta T_i}{\sigma_{\Delta T_i}} \right\| + \sum_{i=S, ScS} \left\| \frac{\Delta A_i}{\sigma_{\Delta A_i}} \right\| + \sum_{i=S, ScS} \left\| \left(1 - \frac{\int_{t_1}^{t_2} u_{obs}(t) u_{syn}(t - \tau) dt}{\sqrt{\int_{t_1}^{t_2} u_{obs}(t) dt \int_{t_1}^{t_2} u_{syn}(t) dt}} \right) / \sigma_{DC_i} \right\| \quad (1)$$

where i and j correspond to the phase and event indices, respectively, and ΔT_i and ΔA_i account for the misfits in the ΔT and ΔA measurements, respectively, from the S and ScS phases between the observed u_{obs} and synthetic u_{syn} data sets. The numerator in the third term evaluates the degree of waveform dissimilarity between u_{obs} and u_{syn} according to the so-called decorrelation coefficient (DC), which is defined as one minus the normalized cross-correlation coefficient (CC) between u_{obs} and u_{syn} , wherein τ is the time shift at which the cross-correlation coefficient attains its maximum. The waveform window is defined by t_1 and t_2 , which indicate the starting and ending times that are defined as 10 s prior to and after the phase arrival time, respectively. Each of the ΔT_i , ΔA_i , and DC quantities are dimensionless following normalization with their standard deviations, which are $\sigma_{\Delta T_i}$, $\sigma_{\Delta A_i}$, and σ_{DC} , respectively.

In Figure 3b, we display the three misfit terms for each of the models (i.e., the PREM, the LLNL model, and our preferred models) with three sets of bars, namely, ΔT is shown in blue, ΔA is shown in red, and the CC is shown in green. After conducting the grid search, we obtain two models (Models I and II in Figure 3b) that reveal depths for the TB of the fragment that are the shallowest depth of the HVSL anomaly (300 km and 500 km, respectively). The traveltime and waveform fits improve significantly, but the improvement in the amplitude fit is minor. The misfit in the amplitude anomalies may be attributable to the susceptibility of the wave amplitude to scattering and the attenuation effects sourced from heterogeneities in the Earth's interior, suggesting that regional large-amplitude variations cannot be modeled under a 2-D structure approximation. For example, a shallow structure, such as a thick sedimentary basin beneath a receiver, will affect the waveform amplitude. Note that the misfits remain relatively high but stable, that is, the largest misfits in the amplitude are nearly constant, which implies that the slab effects are mainly sensitive to the traveltime and the waveform shapes. In summary, while the misfit errors remain large, the slab structure can be resolved. In particular, in Figures 3c–3e, we display three sets of misfit surfaces from the grid search. Our inversion results suggest that for greater slab depths, gentler dip angles are required to fit the data (Figure 3c). The embedded HVSL anomaly with a TB located at a depth of either 300 km or 500 km can return an equally good fit for the observed waveforms. Considering the combined effects of the sharpness and width (Figure 3d), our optimal model prefers a 100 km thick fast core with tapered edges that are ~50 km thick along both sides. The severe trade-off between the velocity perturbation and the length of the structure is expected because of the complementary effects of these two parameters. However, by jointly inverting the

model parameters from five separate events at different distances, these trade-offs can be largely mitigated (Figure 3e).

Examples of waveforms that are fit to the stacked observations are presented in Figure 4. Note that the clearest multipathing occurs for events with the shortest durations (Figure 4b). Although our preferred model readily explains most of our observations, there are still significant fluctuations in ΔA and ΔT for the ScS phases recorded by stations between 73° and 77° from the event (2012.149) with the farthest distance (Figure 1). The anomalous traveltimes in the ScS arrivals disappear for the closer events, which implies that the source of the low-velocity anomaly is situated within the lower mantle. Recently, Ko et al. (2017) reported a pile-like low-velocity structure (PLVS) underneath a fast slab below northern South America (Figure 3a). The proposed location of this PLVS is well correlated with the ScS bounce points at the core-mantle boundary (CMB), which are delayed for the raypaths from event 2012.149. In conjunction with an anomalous lower mantle structure, the simulated waveforms can not only capture the first-order patterns of the traveltimes and amplitude anomalies (Figure S6) but also recover the waveform complexities induced by the sharp edges of the HVSL structure.

4. Discussion

While we are able to identify a subducted, embedded, dipping HVSL structure beneath the southeastern U.S., the true dip of the HVSL anomaly is difficult to resolve with only one azimuthal sample (i.e., with a 2-D section) because of the trade-off in the strike and dip values. The uncertainty in the dipping angle may also affect our estimates of the fragment sharpness and the amplitude of the HVSL. However, clear observations of multiple arrivals (red circles in Figure 2b) are strongly correlated with the alignment between the edges of the HVSL and the event raypaths. If the raypaths do not align well with the edges of the HVSL, we expect a sharper, higher-amplitude resolution of the edges of the fragment (Sun & Helmberger, 2011). Hence, we suggest that the sharpness of the HVSL as defined in this study should constitute a valid feature. Moreover, our inversion results suggest two HVSL structure models with TB depths of either 300 km or 500 km can readily explain the data. However, there is evidence for a well-developed seismic discontinuity at a depth of 290 km with a positive 3% *P* wave velocity anomaly (Chu, Schmandt, et al., 2012) at a location that is in agreement with the results of this study (Figure 2). Thus, the model with a TB depth of 300 km appears to be preferred. Future studies utilizing earthquakes with better azimuthal and distance ranges at regional epicentral distances may provide better constraints on the true dip and TB depth of the structure. Because of the well-known changes in viscosity at 660 km encountered by sinking slab-like segments, we expect considerable changes in both the velocity and thickness of the fragment. It is likely that the shape of the HVSL structure will become complex as it crosses the transition zone, which could present a problem for our simple parameterization. Further 3-D simulations are necessary for better understanding the detailed 3-D morphology of this HVSL body, especially the portion in the transition zone.

4.1. The Origin of the HVSL

Many studies have identified the HVSL anomaly beneath the southeastern U.S., but its origin is still unclear. Two competing scenarios have been proposed involving the subduction of the Farallon Plate (FAR) (Liu et al., 2010; Porritt et al., 2014; Schmandt & Lin, 2014) and the removal of lithospheric material (Biryol et al., 2016).

A general consensus has been reached that the FAR previously subducted beneath the western margin of the North American Plate and is currently forming a complex, dipping wall reaching the CMB beneath the eastern U.S. (i.e., Grand, 2002). The present-day position of the FAR is indicated by a north-south trending high-velocity region (Figure 1a). By combining plate kinematic reconstructions with inverse models of mantle convection patterns, Liu et al. (2010) discussed the role of oceanic plateau subduction on the generation of both the FAR wall and the associated Laramide orogeny. They argued that the subduction of the Shatsky and Hess Conjugate plateaus (SC and HC, respectively), which were located atop the FAR (Figure S7). These authors used inverse models of mantle convection patterns to migrate the high-velocity region back in time for a comparison of the positions of the SC and HC when they encountered the western boundary of the North American Plate. Using a recent plate reconstruction (Müller et al., 2008), they assumed that the SC and HC traveled with the FAR and constructed images of their positions over geological time. They predicted (as shown in Figure S7) that the HC is currently positioned in the mantle beneath the Gulf of Mexico (GOM),

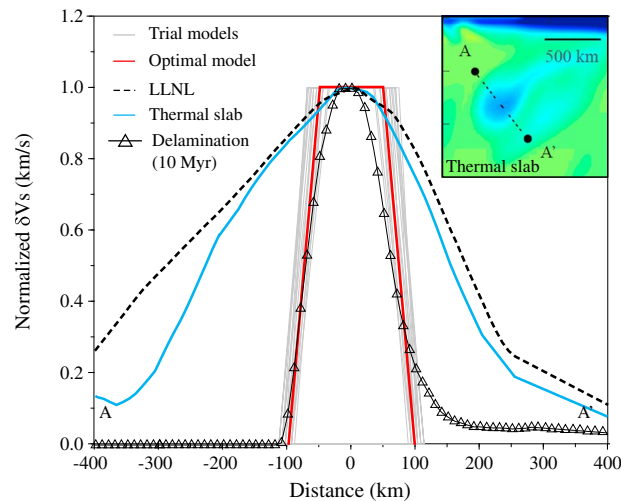


Figure 5. Comparisons of the velocity gradient of the HVSL anomaly estimated using the LLNL model (black dashed line), our preferred model (red line), a geodynamic slab model (blue line), and a geodynamic delamination model at 10 Myr (line with triangles) (Wang & Currie, 2015). The gray background lines indicate all of the possible models that deviate from the optimal solution by less than 5%. The inset shows the cross section of the thermal slab model (Figure S8). AA' represents the profile used to measure the velocity gradient.

which agrees quite well with the position of the HVSL structure from our results. Moreover, in the recent global forward mantle convection model with paleogeographical constraints, the predicted HC localizes below the northern GOM, which also coincides with our estimate of the HVSL structure (Figure S8).

Biryol et al. (2016) proposed an alternative scenario to explain the presence of the HVSL anomaly that is associated with the gravitational removal of lithospheric materials rather than the subduction of the FAR. Although the controlling factors on delamination are still unclear, the gravitationally assisted delamination of the mantle lithosphere has been inferred from various surface observations, including magmatism and anomalous surface deflections (e.g., Elkins-Tanton, 2005, Kay & Kay, 1993, West et al., 2009). One strong line of supporting evidence for a delamination scenario in this region is an anomalously thin lithosphere that is detected near the surface (Biryol et al., 2016). Partial melting induced via lithospheric delamination can also help to explain the intraplate volcanism observed in this study area (e.g., Biryol et al., 2016, Mazza et al., 2014).

4.2. The Effective Thickness of the HVSL

Both of the abovementioned scenarios appear to explain the HVSL to some extent. However, most previous interpretations heavily rely on tomographic imagery. As we suggested earlier, tomographic images alone cannot discriminate between delaminated lithospheric materials and subducted slab materials, as both constitute very similar seismic signatures. The sharpness of the structure, on the other hand, can help to differentiate between these possible origins.

We display our results for the normalized S wave velocity anomaly of the HVSL structure in Figure 5 along with a comparison of the predictions from various tomographic and geodynamic models. The results from the LLNL model and the HVSL cross section are acquired along the profile AA' in Figure 3a (inset), which is approximately 800 km wide with a central depth of 900 km. The temperature fields of the slab and ambient mantle (inset of Figure 5) were derived from a global mantle convection model (Figure S8), which incorporates paleogeographic constraints on the surface velocity fields (Bower et al., 2015). The predicted thermal structures of the slab from this numerical model (Figure S8) agree well with those generated from the LLNL model, but they do not fit our optimal HVSL model (Figure 5). One way to sharpen the velocity gradient of the dynamically thermal slab is to consider variations in the chemical composition of the anomaly. As mentioned earlier, a localized dynamic subsidence in the GOM from the Paleocene can be attributed to the eclogitized HC (Figure S8). Since the thickness of the oceanic crust beneath an oceanic plateau (i.e., the HC and SC) is 4–5 times thicker than that of a normal oceanic plate (i.e., Korenaga & Sager, 2012, Vallier et al., 1983), we expect that the basalt-eclogite transition in the HC during its subduction could have led to not only a density anomaly but also a seismically detectable velocity anomaly (i.e., Williams & Revenaugh, 2005). Such

a complex density anomaly embedded within the FAR could have formed a possible substructure (i.e., an HVSL) with an apparent strike and dip that are different from that of the FAR.

In contrast to the subduction scenario, we also consider the recently predicted generic delamination structure from Wang and Currie (2015) for a comparison with the HVSL structure (Biryol et al., 2016). The negative buoyancy due to the thermal contraction could drive delamination of continental lithosphere in a cratonic region, even though the lithospheric mantle is regarded as depleted in iron (Song & Helmberger, 2007a, 2007b). But the negative buoyancy may not be strong enough to allow the delaminated lithosphere to sink into the lower mantle. We compared the simulated thermal structure of a delaminated mantle lithosphere 10 Myr after its removal from the upper plate (Wang & Currie, 2015) (Figure 5). The effects of thermal diffusion by the ambient mantle on the delaminated materials are not severe because of its relatively short time in the convective mantle; thus, the fragment can still produce a sharp velocity gradient (Figure 5). If the delaminated materials stay in sublithospheric mantle for a longer period, the thermal diffusion would gradually smooth out the boundaries. Even though our model with sharp edges is consistent with the lithospheric delamination scenario if purely thermal effects are considered, it is unlikely for the delaminated materials to sink to ~900 km depth within 10 Myr, considering the average sinking rate is 1.3 ± 0.3 cm/yr for the whole mantle (Butterworth et al., 2014).

In summary, the depths (~900 km) and sharpness of the anomaly suggest that the HVSL is resulted from the eclogitized Hess conjugate that embedded within the Farallon Plate. The basalt-eclogite phase change in the thick Hess conjugate crust not only contributes to the subsidence in the GOM in the Cenozoic (Figure S8) but also significantly elevates the seismic velocity gradients.

5. Conclusion

We have demonstrated the existence of a HVSL structure penetrating into the lower mantle. Its location and geometry are inferred from systematic patterns of the waveform distortions of the S and ScS phases from five events. An inversion of these data reveals two solutions depending on the TB depth and the dipping angle (i.e., 300 km, 50° and 500 km, 40°). The length of the fragment is 1,000 km, and it is characterized by a velocity increase of 2.5%. The core has a thickness of approximately 100 km and exhibits relatively sharp edges (i.e., a 50 km transition thickness). Such sharp edges may favor the fast sinking of delamination materials if purely thermal effects are involved, but the depths (~900 km) of the anomaly suggest an unrealistic sinking rate of the delaminated mantle lithosphere within 10 Myr. Alternatively, the HVSL structure could be part of the broad, eastward subducting FAR. In this scenario, the HVSL structure would have been caused by the subduction of the HC, thereby representing a thermal and chemical origin. Future in-depth geodynamic and high-resolution waveform modeling of the transition structure can hopefully image this HVSL fragment with a better resolution of its structural morphology, thereby increasing our understanding of plate dynamics and our appreciation of surface tectonics.

Acknowledgments

We thank Nathan Simmons, who provided the newest global model used for the FD simulations, and the IRIS DMC (<http://ds.iris.edu/ds/nodes/dmc/>), which provided the earthquake waveform data used in our study. Suggestions and comments were provided by the Editor (Jeroen Ritsema), a reviewer (Daniel A. Frost), and an anonymous reviewer that helped to improve our manuscript. We also thank Priscilla McLean for her help in preparing this manuscript. This work was supported by the NSF CSEDI program.

References

- Biryol, C. B., Wagner, L. S., Fischer, K. M., & Hawman, R. B. (2016). Relationship between observed upper mantle structures and recent tectonic activity across the Southeastern United States. *Journal of Geophysical Research: Solid Earth*, *121*, 3393–3414. <https://doi.org/10.1002/2015JB012698>
- Bower, D. J., Gurnis, M., & Flament, N. (2015). Assimilating lithosphere and slab history in 4-D earth models. *Physics of the Earth and Planetary Interiors*, *238*, 8–22.
- Bunge, H.-P., & Grand, S. (2000). Mesozoic plate-motion history below the northeast Pacific Ocean from seismic images of the subducted Farallon slab. *Nature*, *405*, 337–340.
- Butterworth, N., Talsma, A., Müller, R., Seton, M., Bunge, H.-P., Schubert, B., ... Heine, C. (2014). Geological, tomographic, kinematic and geodynamic constraints on the dynamics of sinking slabs. *Journal of Geodynamics*, *73*, 1–13.
- Chen, M., Liu, Q., Tromp, J., Helmberger, D., & Kanamori, H. (2006). Waveform modeling and 3-D finite-frequency kernels in the Japan subduction zone. Abstract S41B-1329 Presented at the 2006 AGU Fall Meeting, San Francisco, CA, 11–15 Dec. Retrieved from <http://abstractsearch.agu.org/meetings/2006/FM/S41B-1329.html>
- Chu, R., Helmberger, D. V., & Gurnis, M. (2012). Upper Mantle Surprises derived from the recent Virginia Earthquake waveform data. *Earth and Planetary Science Letters*, *402*, 167–175. <https://doi.org/10.1016/j.epsl.2012.10.023>
- Chu, R., Schmandt, B., & Helmberger, D. V. (2012). Juan de Fuca subduction zone from a mixture of tomography and waveform modeling. *Journal of Geophysical Research*, *117*, B03304. <https://doi.org/10.1029/2012JB009146>
- Dziewonski, A. M., & Anderson, D. L. (1981). Preliminary reference Earth model (PREM). *Physics of the Earth and Planetary Interiors*, *25*, 297–356.
- Dziewonski, A. M., Chou, T.-A., & Woodhouse, J. H. (1981). Determination of earthquake source parameters from waveform data for studies of global and regional seismicity. *Journal of Geophysical Research*, *86*, 2825–2852. <https://doi.org/10.1029/JB086iB04p02825>

- Eikström, G., Nettles, M., & Dziewonski, A. M. (2012). The global CMT project 2004–2010: Centroid-moment tensors for 13,017 earthquakes. *Physics of the Earth and Planetary Interiors*, 200–201, 1–9. <https://doi.org/10.1016/j.pepi.2012.04.002>
- Elkins-Tanton, L. T. (2005). Continental magmatism caused by lithospheric delamination. *Special Paper of the Geological Society of America*, 388, 449–461.
- Grand, S. P. (2002). Mantle shear-wave tomography and the fate of subducted slabs. *Philosophical transactions of the Royal Society of London: Series A*, 360, 2475–2491.
- Helmberger, D. V., Engen, G., & Grand, S. (1985). Notes on wave-propagation in Laterally Varying Structure. *Journal of Geophysics-Zeitschrift Fur*, 58(1–3), 82–91.
- Jones, C. H., Kanamori, H., & Roecker, S. W. (1994). Missing roots and mantle “drips”: Regional Pn and teleseismic arrival times in the southern Sierra Nevada and vicinity, California. *Journal of Geophysical Research*, 99(B3), 4567–4601. <https://doi.org/10.1029/93JB01232>
- Kawai, K., Takeuchi, N., & Geller, R. J. (2006). Complete synthetic seismograms up to 2 Hz for transversely isotropic spherically symmetric media. *Geophysical Journal International*, 164, 411–424.
- Kay, R. W., & Kay, S. M. (1993). Delamination and delamination magmatism. *Tectonophysics*, 219, 177–189.
- Ko, J. Y.-T., Hung, S.-H., Kuo, B.-Y., & Zhao, L. (2017). Seismic evidence for the depression of the D discontinuity beneath the Caribbean: Implication for slab heating from the Earth’s core. *Earth and Planetary Science Letters*. <https://doi.org/10.1016/j.epsl.2017.03.032>
- Korenaga, J., & Sager, W. W. (2012). Seismic tomography of Shatsky Rise by adaptive importance sampling. *Journal of Geophysical Research*, 117, B08102. <https://doi.org/10.1029/2012JB009248>
- Levander, A. R. (1988). Fourth-order finite-difference P-SV seismograms. *Geophysics*, 53(11), 1425–1436.
- Li, D., Helmberger, D. V., Clayton, R., & Sun, D. (2014). Global synthetic seismograms using a 2D finite-difference method. *Geophysical Journal International*, 197(2), 1166–1183.
- Li, D., Sun, D., & Helmberger, D. (2014). Notes on the variability of reflected inner core phases. *Earthquake Science*, 27(4), 441–468.
- Liu, L., Gurnis, M., Seton, M., Saleeby, J., Müller, R. D., & Jackson, J. M. (2010). The role of oceanic plateau subduction in the Laramide orogeny. *Nature Geoscience*, 3, 353–357.
- Liu, L., Spasojevic, S., & Gurnis, M. (2008). Reconstructing Farallon plate subduction beneath North America back to the Late Cretaceous. *Science*, 322, 934–938.
- Lu, C., & Grand, S. P. (2016). The effect of subducting slabs in global shear wave tomography. *Geophysical Journal International*, 205(2), 1074–1085. <https://doi.org/10.1093/gji/ggw072>
- Mazza, S. E., Gazel, E., Johnson, E. A., Kunk, M. J., McAleer, R., Spotila, J. A., ... Coleman, D. S. (2014). Volcanoes of the passive margin: The youngest magmatic event in eastern North America. *Geology*, 42, 483–486.
- Müller, R. D., Sdrolias, M., Gaina, C., Steinberger, B., & Heine, C. (2008). Long-term sea level fluctuations driven by ocean basin dynamics. *Science*, 319, 1357–1362.
- Porritt, R. W., Allen, R. M., & Pollitz, F. F. (2014). Seismic imaging east of the Rocky Mountains with USArray. *Earth and Planetary Science Letters*, 402, 16–25. <https://doi.org/10.1016/j.epsl.2013.10.034>
- Ritsema, J., Deuss, A., van Heijst, H. J., & Woodhouse, J. H. (2011). S40RTS: A degree-40 shear-velocity model for the mantle from new Rayleigh wave dispersion, teleseismic travel time and normal-mode splitting function measurements. *Geophysical Journal International*, 184, 1223–1236.
- Saleeby, J., Le Pourhiet, L., Saleeby, Z., & Gurnis, M. (2012). Epirogenic transients related to mantle lithosphere removal in the southern Sierra Nevada region, California, part I: Implications of thermomechanical modeling. *Geosphere*, 8(6), 1286–1309.
- Schmandt, B., & Lin, F. C. (2014). P and S wave tomography of the mantle beneath the United States. *Geophysical Research Letters*, 41, 6342–6349. <https://doi.org/10.1002/2014GL061231>
- Sigloch, K., & Mihalyuk, M. G. (2013). Intra-oceanic subduction shaped the assembly of Cordilleran North America. *Nature*, 496, 50–56.
- Silver, P. G., & Chan, W. W. (1986). Observations of body wave multipathing from broadband seismograms: Evidence for lower mantle slab penetration beneath the Sea of Okhotsk. *Journal of Geophysical Research*, 91, 13,787–13,802. <https://doi.org/10.1029/JB091iB14p13787>
- Simmons, N. A., Myers, S. C., Johannesson, G., & Matzel, E. (2012). LLNL-G3Dv3: Global P wave tomography model for improved regional and teleseismic travel time prediction. *Journal of Geophysical Research*, 117, B10302. <https://doi.org/10.1029/2012JB009525>
- Simmons, N. A., Myers, S. C., Johannesson, G., Matzel, E., & Grand, S. P. (2015). Evidence for long-lived subduction of an ancient tectonic plate beneath the southern Indian Ocean. *Geophysical Research Letters*, 42, 9270–9278. <https://doi.org/10.1002/2015GL066237>
- Song, T. R. A., & Helmberger, D. V. (2007a). Validating tomographic model with broad-band waveform modelling: An example from the LA RISTRA transect in the southwestern United States. *Geophysical Journal International*, 171, 244–258.
- Song, T. R. A., & Helmberger, D. V. (2007b). A depleted, destabilized continental lithosphere near the Rio Grande rift. *Earth and Planetary Science Letters*, 262, 175–184. <https://doi.org/10.1016/j.epsl.2007.07.052>
- Sun, D., & Helmberger, D. V. (2011). Upper-mantle structures beneath USArray derived from waveform complexity. *Geophysical Journal International*, 184(1), 416–438.
- Tromp, J., Komatitsch, D., Hjörleifsdóttir, V., Liu, Q., Zhu, H., Peter, D., ... Hutko, A. (2010). Near real-time simulations of global CMT earthquakes. *Geophysical Journal International*, 183(1), 381–389.
- Tromp, J., Komatitsch, D., & Liu, Q. (2008). Spectral-element and adjoint methods in seismology. *Communications in Computational Physics*, 3(1), 1–32.
- Vallier, T. L., Dean, W. E., Rea, D. K., & Thiede, J. (1983). Geologic evolution of Hess Rise, central North Pacific Ocean. *Geological Society of America Bulletin*, 94(11), 1289–1307.
- Vidale, J., Helmberger, D. V., & Clayton, R. W. (1985). Finite-difference seismograms for SH waves. *Bulletin of the Seismological Society of America*, 75(6), 1765–1782.
- Wang, H., & Currie, C. A. (2015). Magmatic expressions of continental lithosphere removal. *Journal of Geophysical Research: Solid Earth*, 120, 7239–7260. <https://doi.org/10.1002/2015JB012112>
- West, J. D., Fouch, M. J., Roth, J. B., & Elkins-Tanton, L. T. (2009). Vertical mantle flow associated with a lithospheric drip beneath the Great Basin. *Nature Geoscience*, 2, 438–443.
- Williams, Q., & Revenaugh, J. (2005). Ancient subduction, mantle eclogite, and the 300 km seismic discontinuity. *Geology*, 33(1), 1–4. <https://doi.org/10.1130/G20968.1>
- Zhan, Z., Helmberger, D. V., & Li, D. (2014). Imaging subducted slab structure beneath the Sea of Okhotsk with teleseismic waveforms. *Physics of the Earth and Planetary Interiors*, 232, 30–35.